ADVANCED MATERIALS
www.advmat.de

A Naturally Inspired Extrusion-Based Microfluidic Approach for Manufacturing Tailorable Magnetic Soft Continuum Microrobotic Devices

Lukas Hertle, Semih Sevim, Jiawei Zhu, Vitaly Pustovalov, Andrea Veciana, Joaquin Llacer-Wintle, Fabian C. Landers, Hao Ye, Xiang-Zhong Chen, Hannes Vogler, Ueli Grossniklaus, Josep Puigmartí-Luis, Bradley J. Nelson,* and Salvador Pané**

Soft materials play a crucial role in small-scale robotic applications by closely mimicking the complex motion and morphing behavior of organisms. However, conventional fabrication methods face challenges in creating highly integrated small-scale soft devices. In this study, microfluidics is leveraged to precisely control reaction-diffusion (RD) processes to generate multifunctional and compartmentalized calcium-cross-linkable alginate-based microfibers. Under RD conditions, sophisticated alginate-based fibers are produced for magnetic soft continuum robotics applications with customizable features, such as geometry (compact or hollow), degree of cross-linking, and the precise localization of magnetic nanoparticles (inside the core, surrounding the fiber, or on one side). This fine control allows for tuning the stiffness and magnetic responsiveness of the microfibers. Additionally, chemically cleavable regions within the fibers enable disassembly into smaller robotic units or roll-up structures under a rotating magnetic field. These findings demonstrate the versatility of microfluidics in processing highly integrated small-scale devices.

1. Introduction

Nature's intricate machineries have long fascinated researchers in engineering and robotics, going all the way back to Leonardo da Vinci.[1–3] From the elongated shapes of pollen tubes[4] to the segmented growth of centimeter-long bacteria,[5] natural engines and mechanisms have inspired the realization of advanced devices and tools. Recent efforts have led to the development of continuum robots, ranging from large-scale devices[6–9] to micrometer-sized endoscopes[10] and catheters,[11,12] designed to navigate challenging environments such as the human body. In striving to create devices that closely mimic the motion mechanisms,[13] the morphing behavior of organisms,[14] and ultimately, their

L. Hertle, S. Sevim, J. Zhu, V. Pustovalov, A. Veciana, J. Llacer-Wintle, F. C. Landers, H. Ye, X.-Z. Chen, B. J. Nelson, S. Pané
Multi-Scale Robotics Lab
Institute of Robotics and Intelligent Systems
ETH Zurich
Tannenstrasse 3, Zurich 8092, Switzerland
E-mail: sevims@ethz.ch; bnelson@ethz.ch; vidalp@ethz.ch

X.-Z. Chen
Institute of Optoelectronics
State Key Laboratory of Photovoltaic Science and Technology
Shanghai Frontiers Science Research Base of Intelligent Optoelectronics and Perception
Fudan University
Shanghai 200433, P. R. China

The ORCID identification number(s) for the author(s) of this article can be found under https://doi.org/10.1002/adma.202402309

DOI: 10.1002/adma.202402309

X.-Z. Chen
Yiwu Research Institute of Fudan University
Yiwu, Zhejiang 322000, China

H. Vogler, U. Grossniklaus
Department of Plant and Microbial Biology & Zurich-Basel Plant Science Center
University of Zurich
Zollikerstrasse 107, Zurich 8008, Switzerland

J. Puigmartí-Luis
Departament de Ciència dels Materials i Química Física
Institut de Química Teòrica i Computacional
University of Barcelona
Martí i Franquès, 1, Barcelona 08028, Spain

J. Puigmartí-Luis
Institució Catalana de Recerca i Estudis Avançats (ICREA)
Pg. Lluís Companys 23, Barcelona 08010, Spain

physicochemical attributes,[15] significant efforts have been dedicated to processing soft materials. These materials include polymers, liquid crystals, colloids, surfactants, bio-derived products, and composites thereof.[16–19] However, processing these materials at small scales presents certain challenges, particularly regarding the customization of devices and the integration of different components. Conventional approaches, such as 3D printing, micromachining, or LIGA (lithography, electroplating, molding) processes fall short in attaining the required level of integration necessary for constructing a multi-component small-scale device capable of meeting all the demands, particularly those essential for operation within the human body.[20]

While nature-inspired material and device design has managed to establish itself firmly,[21–24] its usage as a source of inspiration in manufacturing remains sparse, suffering from the high complexity of its underlying processes. Biological micromachineries exert a superior control over the assembly processes of chemical building blocks in every single component of living organisms, from the tusks of elephants to the tiny membranes and cell walls of microorganisms and cells of multicellular organisms.[25–27] Therefore, manufacturing approaches that can offer an exquisite control over self-assembly are required to achieve highly integrated micro- and nanoscale devices.[28,29] Microfluidics, with its ability to control the assembly of matter,[30–32] holds promise in addressing current limitations in customization and multifunctionality of small-scale machinery. By leveraging the versatility of microfluidics, researchers have demonstrated the capability of fabricating complex microarchitectures with precision and efficiency.[33,34] For example, microfluidic tools have been utilized to process soft multi-material structures at small scales via co-flow assisted phase separation in conjunction with photolithography.[35,36] Furthermore, recent studies have shown that microfluidics can successfully attain the fabrication of complex robotic microarchitectures such as triplex, core–shell, Janus-like, and even double-helix structures.[37–40] Its inherent capability of precise control over the occurring mass transport as well as reaction kinetics during manufacturing, even showed to enable multi-material based micro-structure formation enabling the fabrication of complex heterogeneous tissue bioprinting.[41–45]

In this study, we push the boundaries of microfluidic-based manufacturing by leveraging its precise control over reaction-diffusion (RD) processes to form highly integrated multifunctional hydrogel-based magnetic microfibers (**Figure 1a**). Specifically, we draw inspiration from the growth of plant pollen tubes, a process closely linked to the flux of calcium ions (Ca^{2+}).[46–49] To mimic this phenomenon, we employ alginate hydrogels that cross-link with Ca^{2+} during the manufacturing process. The utilization of RD control facilitated by microfluidics enables us to create sophisticated alginate-based fibers with customizable features, including the geometry (compact or hollow), the stiffness along the fiber (by controlling the Ca^{2+} concentration and nanoparticle (NP) content), and magnetic response based on the precise localization of magnetic NPs (either inside the fiber's core, surrounding the fiber completely or only on one side) (Figure 1b,c). Such precise control over manufacturing allows us to develop multifunctional devices (e.g., decorated with functional NPs and multiple model drugs) that are tailored for magnetic soft continuum robotics applications (Figure 1d). Furthermore, we introduce chemically cleavable regions within the fibers, facilitating their disassembly into smaller robotic units, for example, for easy deployment within the intricate vessels of the human body (Figure 1e). The versatility of these composite fibers—that is, the transformation from magnetic soft continuum robots (mSCRs) into smaller robotic units—and the high biocompatibility of employed materials enable their delivery and implantation using microsurgery tools such as microcatheters or small-scale endoscopes (Figure 1f).

2. Results

2.1. Nature-Inspired Fabrication of Customized Tubular mSCR

To fabricate magnetic soft continuum robots (mSCRs) via a nature-inspired method, we employed a microfluidic approach that allows us to establish controlled RD conditions. Under the effect of a low Reynolds number regime, the utilized microfluidic device was able to replicate nature's RD processes to fabricate tubular mSCRs with customized hydrogel scaffolds. We selected alginate as a candidate scaffold material because of its ability to crosslink with Ca^{2+} ions and to form a biocompatible and biodegradable hydrogel.[50]

We employed a 3D hydrodynamic flow focusing (3D-FF) microfluidic device, equipped with multiple inlets (i.e., the number of inlets ≥5, **Figure 2a**), to achieve an unprecedented control over the mass transport (e.g., alginate, magnetic NPs) and chemical diffusion (e.g., diffusion of Ca^{2+}) during the fiber formation. The device was fabricated by press-fitting a glass capillary tube (inner diameter, ID:1 mm) and two concentric metallic needles into a 3D printed holder that includes inlet holes to introduce the different flows (center, middle, and outer shell flows) into the main channel (Figure 2a). This design allows for the generation of three separated concentric flows for the formation of core–shell alginate fibers. More specifically, the rapid ionic crosslinking of the aqueous sodium alginate solution (0.5–2.5 wt%)—which is flushed through the middle shell flow inlets (inlets 3 and 4)—is accomplished via the spatiotemporally controlled Ca^{2+} diffusion from its surrounding concentric sheath flow—that is formed by utilizing from the outer shell flow inlets (inlets 1 and 2)—inside the main channel. Additionally, pumping the deionized (DI) water from the central flow inlet (inlet 5) allows for the formation of continuous hollow alginate fibers by acting as a non-reactive central stream to generate a concentric hole inside alginate flow. Moreover, the 3D-FF feature prevents interaction of the mSCR with the channel walls ensuring an uninterrupted extrusion and facilitates precise control over its diameter (outer diameter, OD: 300–900 μm; inner diameter, ID: 100–600 μm), as well as wall thickness by regulating the relative flow rates of different streams (e.g., central, middle, and sheath flow, see Figure S1 and Movie S1, Supporting Information). The multiple-inlet configuration and fast switching capabilities of inlet flows (e.g., microfluidic junction points that facilitate sequential switching of the streams from inlets 1 and 2; or inlets 3 and 4; or inlets 5′ and 6) enable exquisite control over the customization of these tubular mSCRs. As seen in Figure 2b–h, spatial control over the in situ integration and localization of magnetic NPs enables the fabrication of customized tubular mSCRs having complex actuation capabilities (i.e., programmable folding/bending, vide infra see Section 2.3).

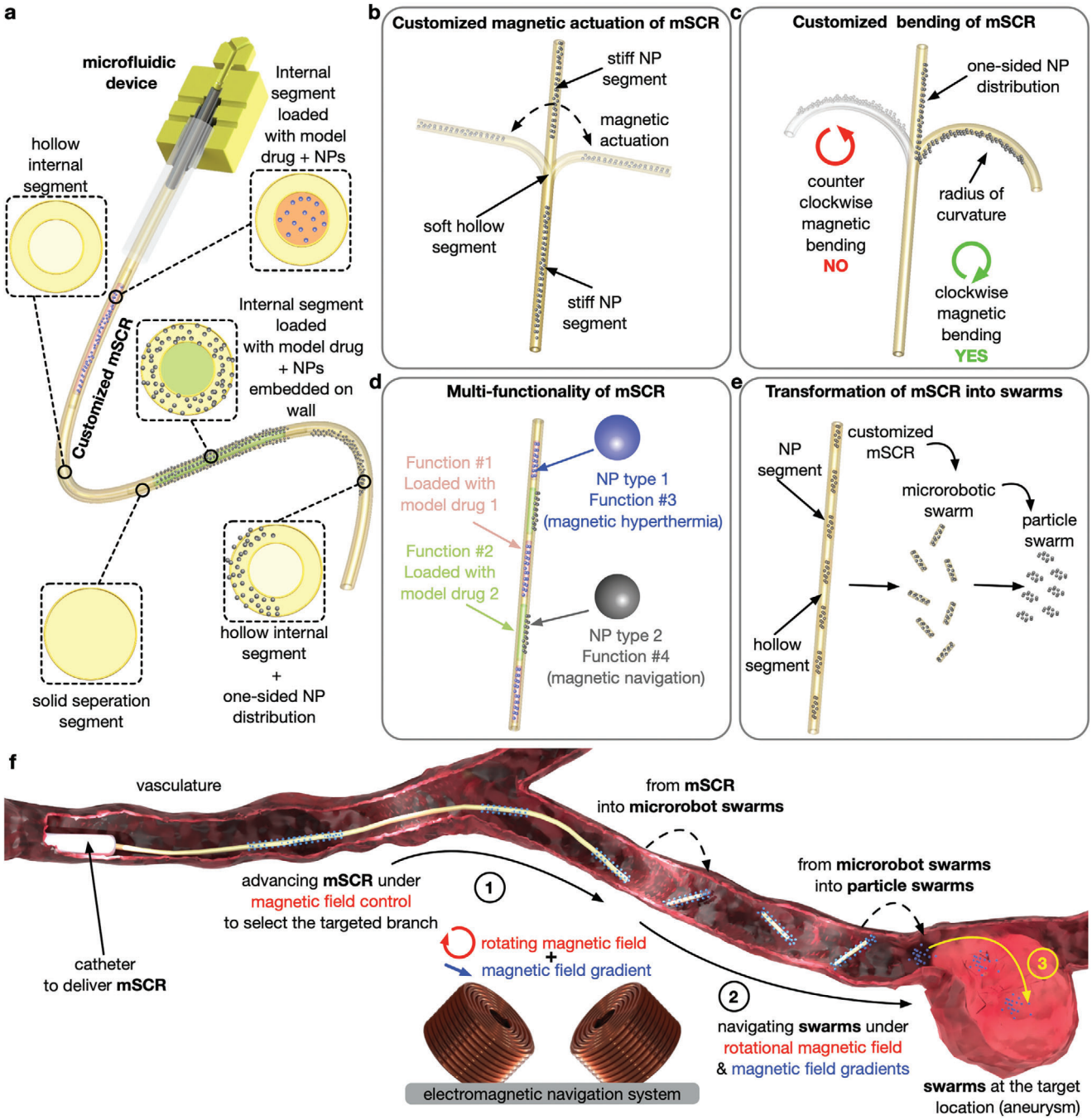

Figure 1. Conceptual illustrations showing the a) fabrication of customized magnetic soft continuum robots (mSCRs); b) customized magnetic actuation achieved via internal compartmentalization of magnetic nanoparticles generating soft and stiff segments; c) programmed bending accomplished by one-sided incorporation of nanoparticles into the wall of mSCR to create preferential and restricted bending directions; d) multi-functionality attained by spatially controlled incorporation of different functional materials (i.e., various kinds of model drugs and nanoparticles); and e) chemically induced transformation of customized mSCRs into swarms. f) The prospective utilization of the customized mSCR in biomedical applications to illustrate its catheter-assisted delivery, magnetic field-assisted navigation, and transformation into smaller robotic swarms that can be navigated toward the target site by applying rotational magnetic field and magnetic field gradients.

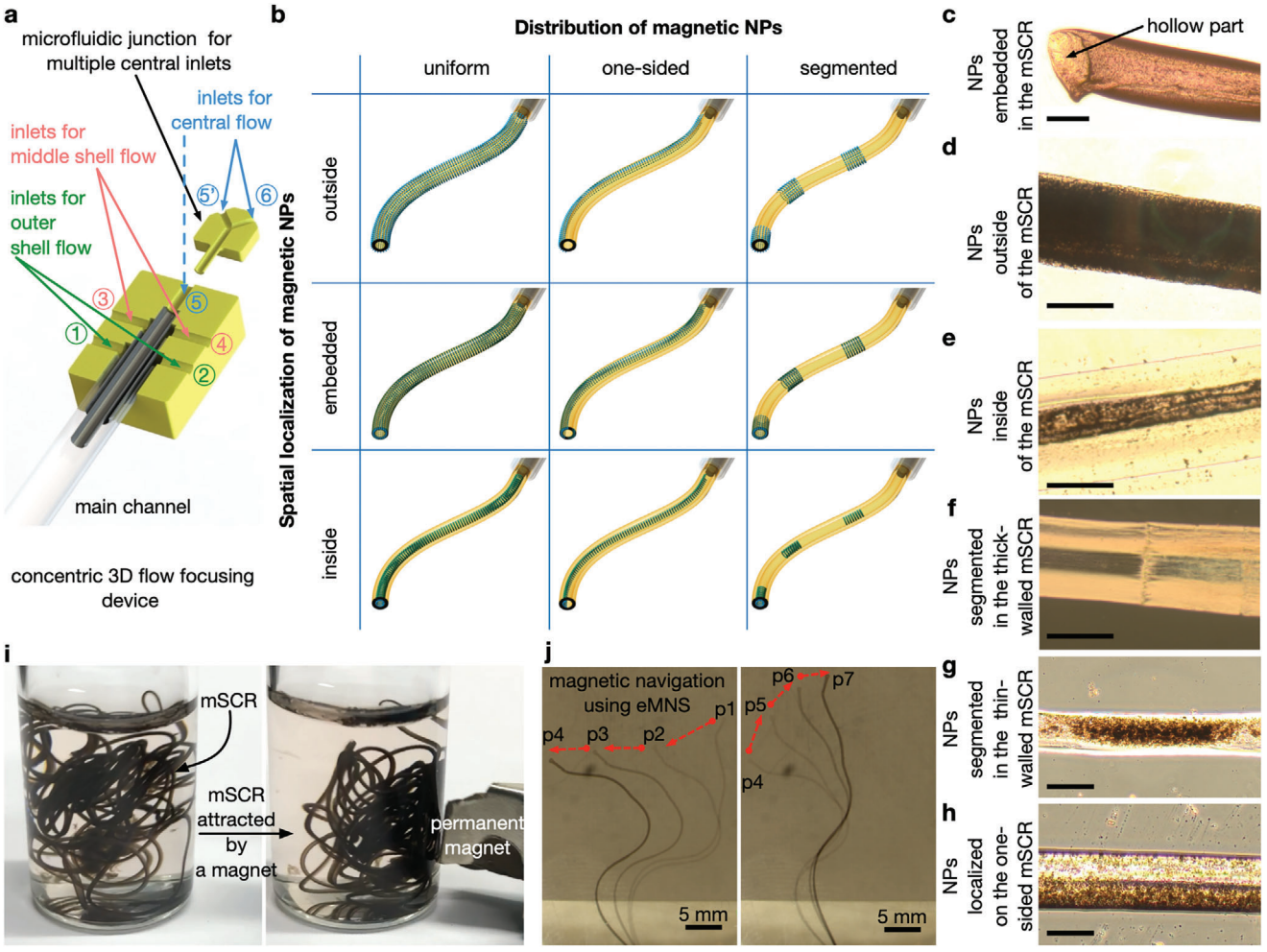

Figure 2. a) CAD model showing the sectional view of the 3D hydrodynamic flow focusing (3D-FF) microfluidic device. The specific inlets to form the concentric core–shell flows are color coded such as outer shell (sheath) flows in green (inlets 1 and 2), middle shell flows in pink (inlets 3 and 4), and central flow in blue (inlet 5 or inlets 5′ and 6). b) Schematic representation showing the control over spatial localization and distribution of magnetic NPs for customizing mSCRs. c–h) Microscope images showing six different kinds of customized mSCRs (scale bars: 200 µm). i) Images showing attraction of mSCRs by a permanent magnet. j) Overlapped time-sequence images showing the magnetic actuation of mSCR using an electromagnetic navigation system (eMNS). Also see Movie S2, Supporting Information.

To fabricate mSCRs, we first synthesized highly crystalline monodispersed iron oxide NPs by means of thermal decomposition in the presence of oleic acid, as described in our previous work.[51] Subsequently, to ensure homogeneous particle dispersion within the alginate polymer matrix, we conducted surface modification by replacing the oleic acid with polyacrylic acid via ligand exchange according to a well-established protocol.[52] Transmission electron microscopy (TEM) images of the synthesized particles confirmed a highly homogeneous cubic particle state with an average diagonal diameter of 23.81 nm (Figure S2a–c, Supporting Information). The crystalline structure of the particles was assessed by X-ray diffraction. The hydrodynamic diameter of the particles after functionalization was determined to be 58.9 nm, and surface modification was confirmed through thermogravimetric analysis (TGA), Fourier-transform infrared (FTIR) spectroscopy, and zeta potential measurements (Figure S3, Supporting Information). Finally, the magnetic characterization of the particles revealed a magnetization of ≈62 emu g^{-1} under an external magnetic field strength of 200 Oe, demonstrating the high magnetic response of mSCRs to magnetic fields and gradients (Figure 2j) and ensuring their precise manipulation using electromagnetic navigation systems (eMNS) (Figure 2j, Movie S2, Supporting Information).

2.2. Mechanical Characterizations of Customized mSCRs

Next, we investigated the mechanical properties of the customized mSCRs to accomplish programmable actuation capabilities under magnetic control. Specifically, the mSCRs were composed of spatially localized magnetic NPs within the alginate matrix crosslinked by divalent Ca^{2+} ions. Therefore, the mSCRs' mechanical properties are directly correlated with the crosslinking density and encapsulated particle concentration. Accordingly, we investigated the local stiffness of mSCRs via indentation experiments.[53,54] Stiffness characterizations of pure

hollow alginate fibers (i.e., without NP incorporation) demonstrated that the hollow fibers crosslinked using five times higher Ca^{2+} concentrations—that is, comparing 10 and 50 mg mL^{-1} Ca^{2+} concentrations—exhibited a 36% higher local stiffness (Figure S4a–c, Supporting Information). The effect of different stiffness based on cross-linking density was also observed during magnetic actuation of mSCRs, with the same particle concentrations but varying cross-linking densities. Specifically, while the soft mSCR crosslinked at low Ca^{2+} concentration (10 mg mL^{-1}) shows an elastic shape change (i.e., its radius of curvature is changing from 119.20 to 26.99 mm, demonstrating 77.4% decrease) under oscillating magnetic field control, the stiffer one crosslinked using a higher Ca^{2+} concentration (20 mg mL^{-1}) exhibited a rigid cantilever beam-like motion (i.e., demonstrating only 3.4% decrease) under the same magnetic control (Figure S4d,e and Movie S3, Supporting Information). Moreover, the stiffness of crosslinked alginate fibers can be increased by almost two orders of magnitude (i.e., from ≈0.3 N m^{-1} up to 25 N m^{-1}) via a dehydration process, whereas re-hydration enables the recovery of the stiffness to ≈165% of its original value (first cycle in Figure S5, Supporting Information). This overall increase in stiffness occurs because of the change in the packing density of the alginate matrix during dehydration and re-hydration. Accordingly, by performing multiple cycles of consecutive dehydration and re-hydration, the stiffness of both states can be gradually increased (compare the first and second cycle in Figure S5, Supporting Information), hence allowing the tailoring of the stiffness of mSCRs even after their microfluidic fabrication. Similarly, we investigated the effect of NP concentration on the stiffness of mSCR. Increasing the NP concentration from 2.5 to 10 mg mL^{-1} results in an ≈70% increase in the local stiffness of mSCRs (Figure S6a–c, Supporting Information). Note that increasing NP concentration shows a significant effect on the distribution of the particles within the alginate matrix as it changes from a homogeneous random particle distribution toward an ordered linear alignment due to the shear-induced alignment[55] of NPs under microfluidic conditions (Figure S6d,e, Supporting Information).

2.3. Programable Actuation of Customized mSCRs

Accordingly, we exploited the spatial control over the in situ integration and localization of magnetic NPs to tailor the stiffness along the length of the mSCRs by creating multiple segments with different stiffness levels (i.e., with and without NPs), thereby emerging programmable magnetic actuation capabilities, such as designed folding points (**Figure 3a**). As observed in Figure 3b, EDX analysis confirmed the controlled localization of iron oxide-based magnetic NPs inside the mSCR, allowing for the generation of soft segments without NPs and stiff segments with magnetic NPs (Movie S4 and Figure S7, Supporting Information). The customized magnetic actuation of mSCRs was evaluated using an eMNS. Remarkably, different customizations performed on the mSCRs result in distinctive steering capabilities under the same magnetic actuation. For example, while the segmented mSCR shows a high bending around the soft alginate segment (i.e., customized folding point), the mSCR with uniformly decorated NPs displays a stiffer, cantilever beam-like deflection (Figure 3c, Movie S4, Supporting Information).

In addition to segmented mSCRs, which are created by adjusting the composition of the central flow using a microfluidic junction to control NP localization along the axial direction, we can also pattern the walls of mSCRs with radially controlled NP distribution to create one-sided mSCRs (Figure S8a–d and Movie S5, Supporting Information). These one-sided mSCRs are fabricated by controlling the relative flow rates and compositions of two inlets (see inlets 3 and 4 in Figure 2a) that are utilized to form the middle shell flow. The resulting asymmetric stiffness and swelling properties on the walls of the mSCRs allow for a programmable bending behavior, ensuring the customized pre-bending of fibers toward the NP decorated side due to the reduced swelling of NP containing alginate matrix (Figure 3d, Figure S9, Supporting Information). The EDX maps confirm that the NPs can be successfully localized on one side of the mSCR, both along its axis and at the cross-section (Figure 3e). This one-sided localization of NPs results in preferred and restricted bending directions. As depicted in Figure 3f, the one-sided mSCR demonstrates preferential clockwise (CW) bending under external magnetic control, while its counter clockwise (CCW) bending is restricted due to the customized localization of NPs (Movie S5, Supporting Information).

More sophisticated mSCR designs can be fabricated by combining internal particle compartmentalization with one-sided lateral NP localization (Figures S8e,S10, and Movie S6, Supporting Information), which provides complex magnetic actuation capabilities. For example, this customization on mSCRs allows for having hook-like shapes to capture and manipulate micrometer- and millimeter-sized soft structures in open spaces inside a liquid medium (Movie S6, Supporting Information), as well as for the successful navigation of mSCRs inside the millimeter-scale close channels (Movie S7, Supporting Information).

2.4. Multifunctionality of Customized mSCRs

Besides programming the actuation abilities of mSCRs, we also demonstrated the multifunctionality of these customized tubular robots. Basically, the hollow part of tubular mSCRs can effectively be compartmentalized for loading various kinds of therapeutic agents, such as multiple drugs (**Figure 4a**). We validated our approach by utilizing chemical dyes as model drugs and demonstrated that different types of dyes (i.e., model drugs) can be loaded inside the mSCRs while avoiding their cross-contamination by localizing alginate walls that separate the different compartments (Figure 4b). By utilizing the various multi-inlet junctions and tailoring the switching times (from the millisecond range up to seconds) for the central flow, we can generate alternating internal segments having different compositions and lengths (Figure S11 and Movie S8, Supporting Information). The combination of this approach with the spatially controlled localization of different magnetic NP types, such as particles with and without hyperthermia capabilities, boosts the functionality of customized mSCRs (Figure 4c,d, Movie S9, Supporting Information). With minor adjustments to the magnetic NP synthesis protocol (as described in Section 2.1), we were able to synthesize octahedron particles with an average size of 12.69 nm (Figures S2d–f and S3, Supporting Information). These particles exhibited a modest decrease in magnetic susceptibility and saturation

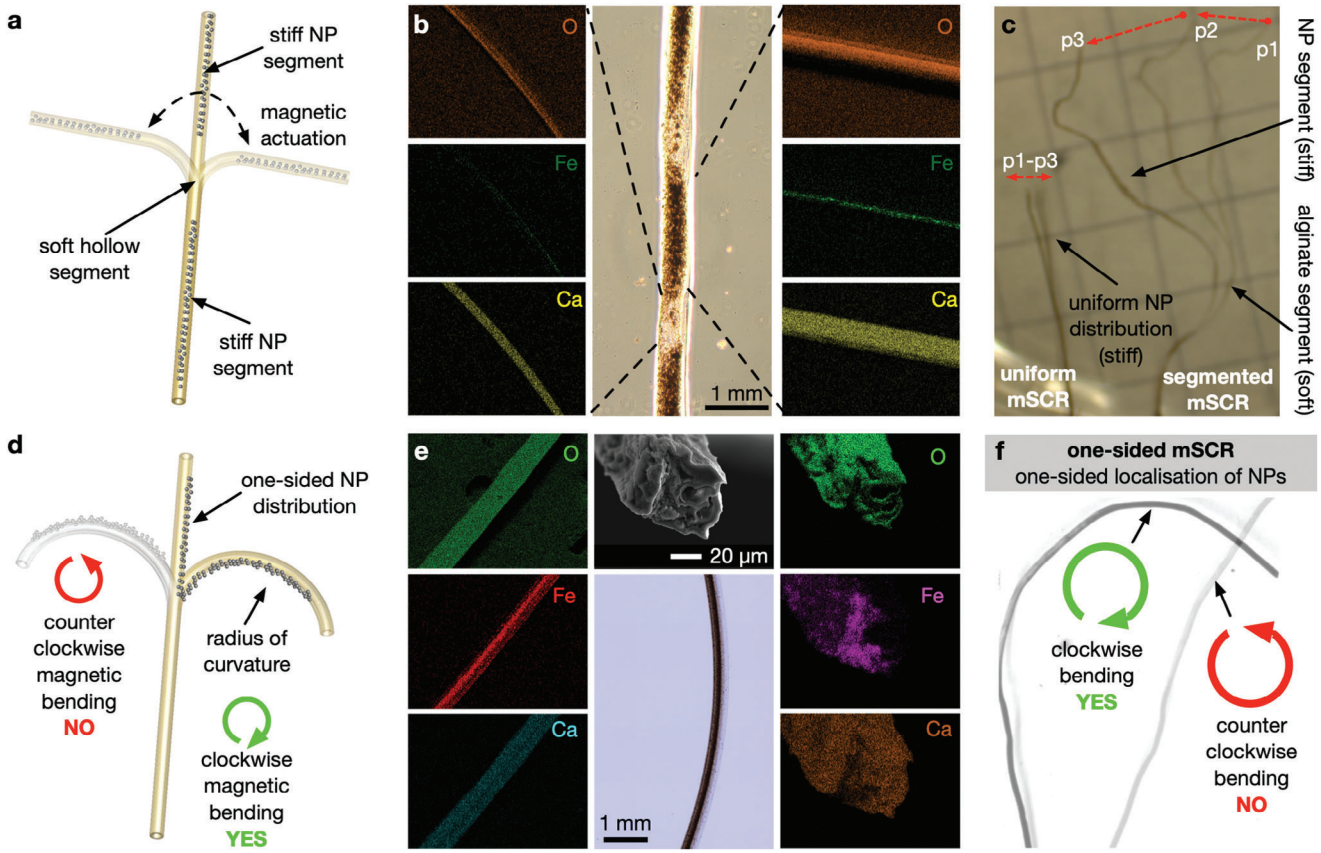

Figure 3. a) Schematic illustration showing the programmed magnetic actuation of segmented mSCR. b) EDX maps showing the elemental distribution of segmented mSCRs. c) Overlapped image sequence to show the distinctive responses obtained from the segmented and uniform mSCRs under the effect of same magnetic actuation. Also see Movie S4, Supporting Information. d) Schematic illustration showing the programmed magnetic bending of one-sided mSCR. e) EDX maps showing the elemental distribution of one-sided mSCRs. f) Overlapped images showing the preferential and restricted bending directions for one-sided mSCR under eMNS actuation. Also see Movie S5, Supporting Information.

magnetization (71 emu g^{-1} compared to 84 emu g^{-1}) at 2T (Figure 4e), most probably caused by surface-related spin canting effects that become increasingly relevant at the nanoscale.[56,57] Additionally, these smaller particles showed a significant decrease in Néel and Brownian relaxation-related heating when exposed to alternating magnetic fields[58] (Figure 4f)—which is characterized by a significantly decreased particle specific loss power (SLP) value of 5 Wg^{-1} compared to cubic particles (SLP = 350 Wg^{-1})—allowing for enhanced customization in the fabrication of compartmentalized mSCRs. While the cubic particles provide an additional functionality, that is, local magnetic heating, the octahedron particles ensure the desired magnetic actuation capabilities of the customized mSCRs without any additional heating.

2.5. Transformation from Customized mSCRs into Microrobot Swarms and Their In Vitro Performance Evaluation

We also demonstrated the successful conversion of customized mSCRs into microrobot swarms using a medically approved Ca^{2+} scavenger, ethylenediaminetetraacetic acid (EDTA),[59] to selectively dissolve the hollow alginate segments (**Figure 5a**). The formation of microrobot swarms from a segmented mSCR was facilitated under rotating magnetic fields (Figure 5c, Movie S10, Supporting Information). Similarly, one-sided mSCRs having a tailored NP distribution (i.e., long segments) could also be transformed into roll-up robots, exploiting the programmable folding capabilities of mSCRs under rotating magnetic fields (Figure 5b,d and Movie S10, Supporting Information).

To assess the feasibility of utilizing produced mSCRs in prospective biomedical applications, we further conducted cell viability tests on HUVEC cell line. All investigated sample types (pure alginate fiber, alginate fiber with internal NP localization, and alginate fiber with NPs embedded in the wall) showed high cell viability after 48 h (Figure S12, Supporting Information), confirming the biocompatible character of the utilized materials.

As seen in Movie S11, Supporting Information, the capability of potential intravascular mSCR deployment was demonstrated in vitro by injecting internally segmented mSCRs (**Figure 6a**) into a human brain vasculature phantom model (Figure 6b) utilizing a catheter tubing as an intermediate delivery-aid (Figure 6c(i)). Under the magnetic control offered by an eMNS, the mSCR's trajectory was successfully steered to reach different vascular target branches (Figure 6c(i–iii)). Specifically, the injection of mSCR in the flow direction ensured a drag originated continuous

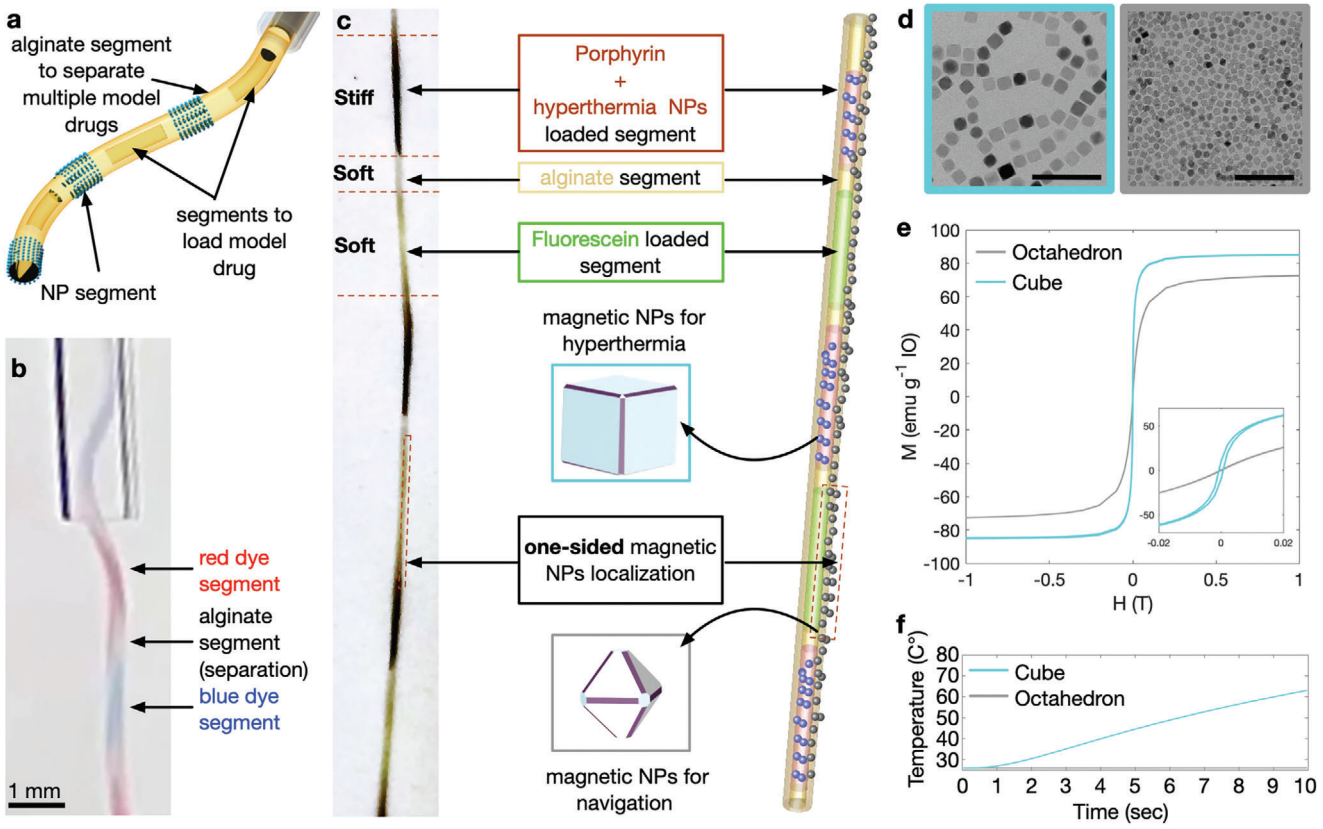

Figure 4. a) Schematic representation of customized mSCR with empty segments to load drugs. b) Proof-of-concept demonstration of loading the mSCR with two different model drugs (red and blue dyes) separated with alginate walls. Also see Movie S8, Supporting Information. c) Multi-functional mSCR loaded with two different model drugs (porphyrin and fluorescein dyes) separated with alginate walls. This multi-functional mSCR was also customized for programmed magnetic actuation and local (segmented) magnetic heating by controlling the spatial localization of two different types of magnetic nanoparticles with and without hyperthermia capabilities. Also see Movie S9, Supporting Information. d) TEM image of different magnetic NPs incorporated in the mSCR presented in panel c. (scale bar: 100 nm) e) VSM results showing the magnetization curves of these NPs (octahedrons and cubes are in grey and light blue, respectively), and f) NP containing DI water solution heating measurements showing the magnetic hyperthermia capabilities of these particles (cubes 50 mg mL^{-1}, octahedron 5 mg mL^{-1}).

forward propulsion (i.e., advancing of the mSCR) along the vasculature branches while bifurcations could be successfully selected (i.e., steering of the mSCR) by applying magnetic field gradients perpendicular to the target direction (Figure 6d(i,ii)). After stopping the flow—which could for example be clinically achieved by the utilization of a balloon catheter—injection of EDTA allowed for the partial dissolution of mSCR (Figure 6d(iii,iv)), hence successfully accomplishing an intravascular microrobot swarm release (Figure 6d(v,vi)). Finally, the transformed swarms were precisely navigated into a targeted aneurism by the application of a combination of magnetic field rotation and gradients (Figure 6d(vii,viii)).

3. Conclusion

In summary, we have effectively utilized microfluidics to precisely control RD processes, forming multifunctional and compartmentalized Ca^{2+} cross-linkable alginate-based mSCRs. By exploiting RD control, we demonstrated the fabrication of sophisticated mSCRs with customizable features, such as tailored geometry (compact or hollow) and stiffness, as well as the precise spatial localization of magnetic NPs in mSCRs. We verified that this precise control allows for tuning the stiffness and magnetic responsiveness of the microfibers, thus facilitating customized magnetic actuation capabilities. We also demonstrated that our method enables the localization of multiple agents within the mSCRs to enhance their multifunctionality. Furthermore, we introduced chemically cleavable regions within the fibers, facilitating their disassembly into smaller robotic units. We envision that our method will open new pathways for the development of multifunctional devices tailored for magnetic soft continuum robotics applications.

4. Experimental Section

Materials: Sodium alginate, calcium chloride, polyacrylic acid, ethylenediaminetetraacetic acid, 1-octadecene, tetradecene, oleic acid, acetone, methanol, tetrahydrofuran, and chloroform were purchased from Sigma Aldrich (Saint Louis, Missouri, USA). Benzyl ether was acquired from Thermo Fisher Scientific Inc. (Waltham, Massachusetts, USA). Iron(III) acetylacetonate was purchased from Across Organics (Geel, Belgium), and sodium oleate from Tokyo Chemical Industry (TCI, Tokyo, Japan). A 3D silicon model of human vasculature was provided by Swiss Vascular.

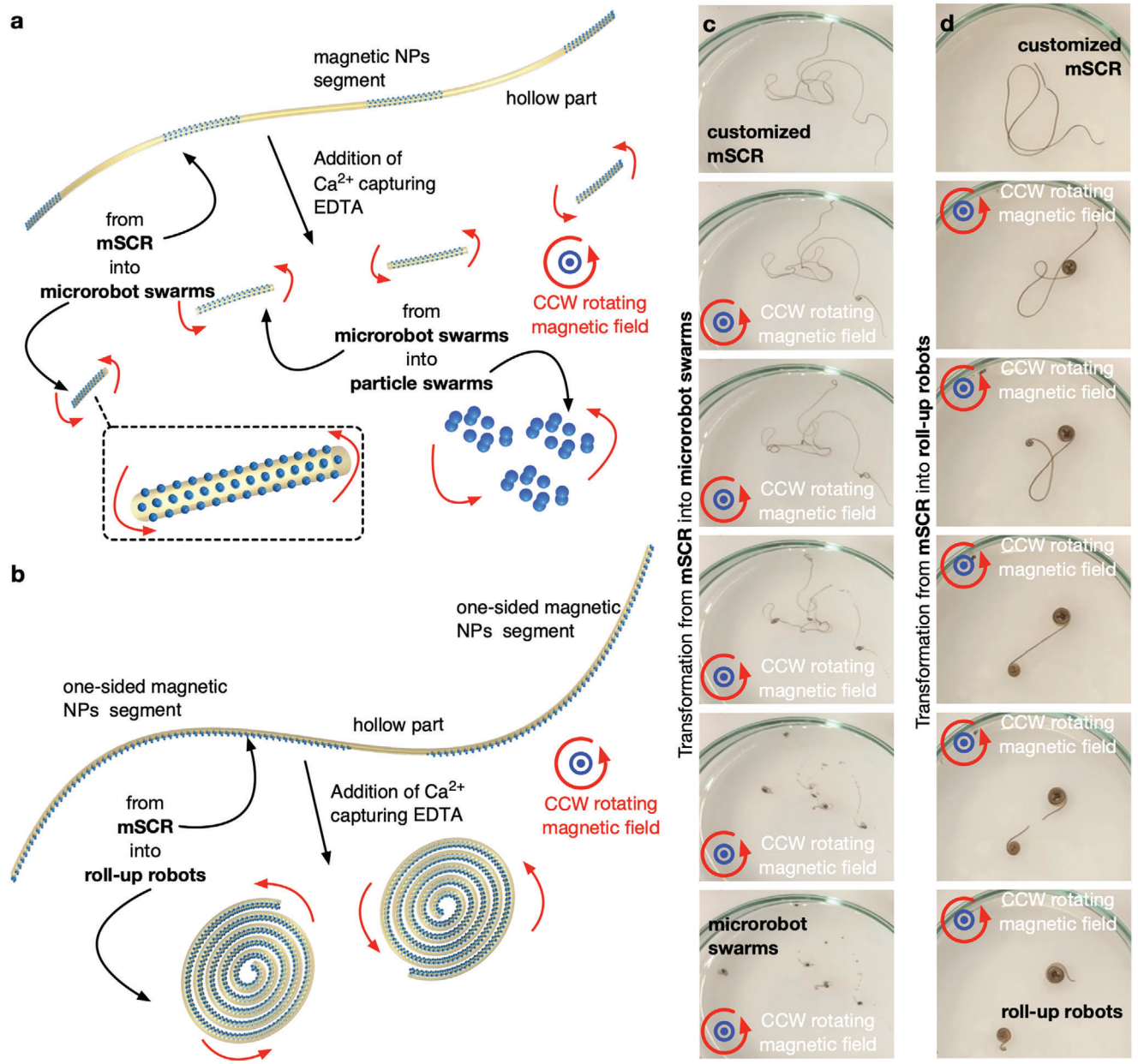

Figure 5. Illustrations showing the transformation of an mSCR into a) a microrobotic swarm and b) roll-up robots. Image sequence showing the transformation of a customized mSCR into c) microrobot swarms and d) roll-up robots under rotating magnetic field. Also see Movie S10, Supporting Information.

Synthesis of Iron Oxide NP Cubes: Magnetic iron oxide nanocubes were synthesized according to a previously reported method.[51] First 540 mg iron(III) acetylacetonate (Fe(acac)3), 1.664 g oleic acid, and 199.6 mg sodium oleate were mixed in a combination of benzyl ether (7 mL), 1-octadecene (15 mL), and tetradecene (3 mL). The reactant slur was subsequently de-gassed for 1 h at 60 °C before getting heated to a reflux at 294 °C under a steady N_2 flow with a heating rate of 3 °C min^{-1}. After refluxing for 90 min, the resulting particle-containing solution was allowed to cool to room temperature before storing it at 4 °C for further processing.

Synthesis of Iron Oxide NP Octahedrons: Small-sized magnetic iron oxide nanooctahedrons were synthesized according to the above-stated protocol (see synthesis of nanocubes) with minor adjustments. First 441 mg of iron(III) acetylacetonate (Fe(acac)3) and 1.854 g oleic were mixed in a combination of benzyl ether (7 mL), 1-octadecene (15 mL), and tetradecene (3 mL). The reactant slur was subsequently de-gassed for 1 h at 90 °C before getting heated to a reflux at 294 °C under a steady N_2 flow with a heating rate of 3 °C min^{-1}. After refluxing for 90 min, the resulting oleic acid coated particle-containing solution was allowed to cool to room temperature before storing it at 4 °C for further processing.

Phase Transfer of Iron Oxide NP: Phase transfer of the synthesized particles followed a previously established method with minor adjustments.[51,52] In the first stage, the as-synthesized iron oxide NPs were purified by washing them in a mixture of chloroform (25 mL) and acetone (75 mL) twice, before twice more redispersing the particles and precipitation in a mixture of methanol (50 mL) and acetone (50 mL). In follow up the purified particles were functionalized with polyacrylic acid

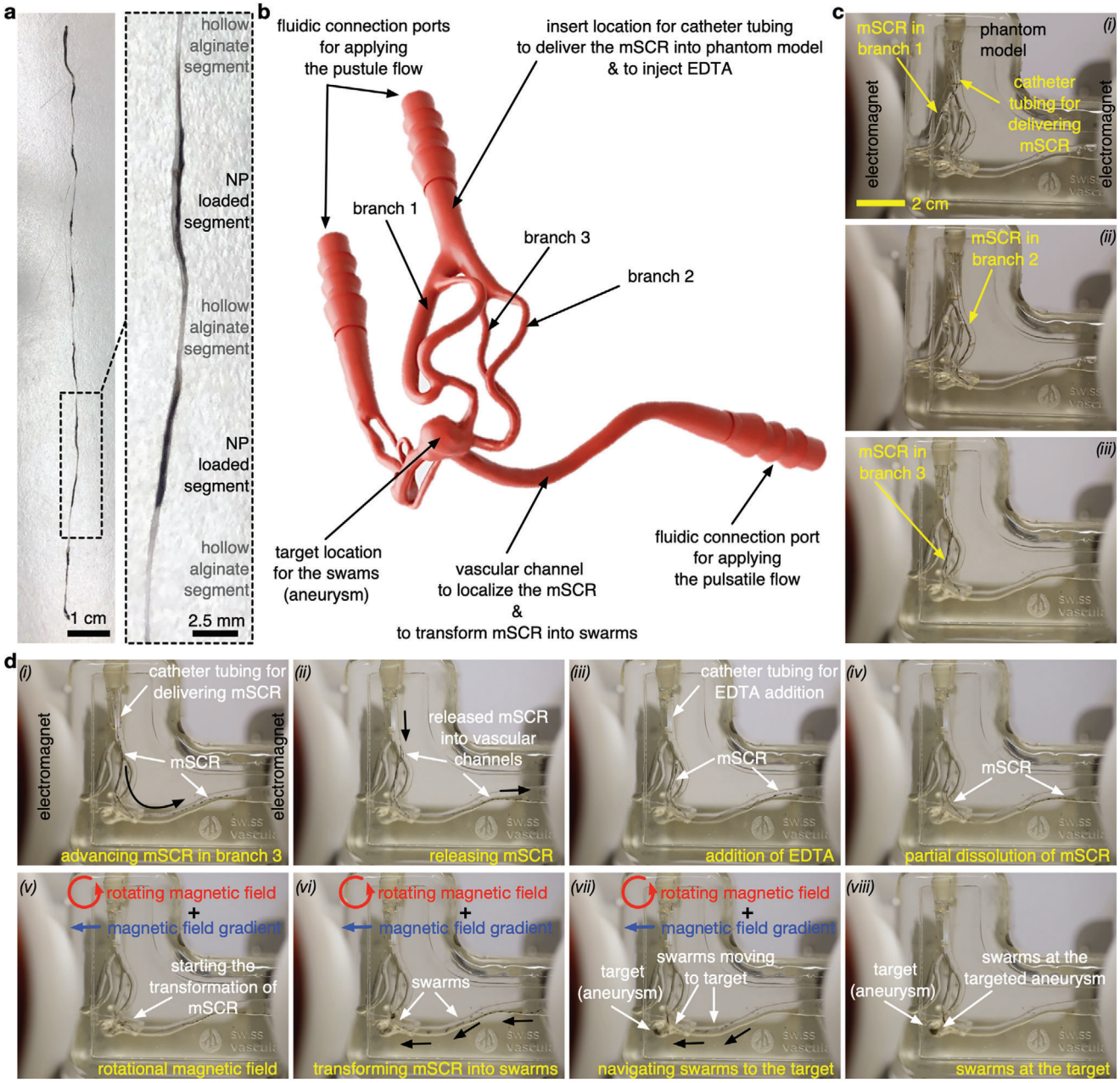

Figure 6. a) The image of internally segmented mSCRs and its magnified version to demonstrate the NP-loaded segments and hollow alginate segments. b) 3D geometry of human brain vasculature model having multiple branches and an aneurysm. c) Images showing the navigation of mSCR (shown in panel (a)) within the silicone human brain vasculature phantom. mSCR that is delivered by employing a catheter tubing successfully reaches all three targeted branches under magnetic control. d) Image sequence showing i) the flow-assisted advancing of mSCR in branch 3 and ii) the release of mSCR; iii) addition of EDTA after stopping the flow and iv) partial dissolution of mSCR; v,vi) transformation of mSCR into swarms; and vii,viii) navigating swarms to the target under the combined effect of rotational magnetic field and magnetic field gradients. Also see Movie S11, Supporting Information.

(PAA). Therefore, 80 mg of oleic acid-coated particles got dispersed in 8 mL of tetrahydrofuran (THF) and added dropwise into 72 mL of 2.88 g PAA-containing THF under vigorous stirring. After being allowed to react for 72 h under a N_2 atmosphere, the PAA-functionalized particles were collected via centrifugation and five times washed by redispersion and sedimentation in de-ionized water. Finally, the particles got dispersed in the desired concentration within DI water having a pH = 5.

Microfluidic Chip Fabrication: The manufacturing of multifluidic Y-junctions and microfluidic device body (i.e., holder part including the inlet ports and holes for press-fitting metallic needles and glass capillaries, see Figure 2a) was performed with a 3D-printer (ProJet MJP 2500 Plus, 3D Systems Inc., Rock Hill, North Carolina, USA), using a transparent resin (VisiJet M2R-CL, 3D Systems Inc., Rock Hill, North Carolina, USA) via multijet printing (MJP). After fabrication, the removal of wax was performed with a MJP EasyClean System (3D Systems Inc., Rock Hill, North Carolina, USA), followed by pressurized steam with a steam gun to eliminate all the casting wax inside the microchannels. Then, two concentric metallic needles (Gauge 27 and Gauge 21) were press-fitted into the holder to shape

concentric center and middle shell flows. Finally, a glass capillary (ID = 1 mm and OD = 1.5 mm) was press-fitted into a holder to form sheath (other shell) flow and the main microfluidic channel.

Synthesis of Soft Continuum Microrobots: Stock solution of alginate (0.25, 0.5, 1, and 2 wt%) was prepared by first suspending the functional component into de-ionized water before the addition of sodium alginate under vigorous stirring. The fabrication of the soft continuum microrobots was subsequently undertaken under continuous flow within custom-made 3D flow-focusing devices connected to a Centoni Nemesys Pump (Centoni GmbH, Korbussen, Germany) operating at flow speed between 100 and 2500 µL min^{-1}, and a Fluigent's Flow EZ pump system (Fluigent, Le Kremlin-Bicêtre, France) operating at pressures between 0.3 and 1.5 bar.

Magnetometry: The magnetic properties of iron oxide NPs were determined by using vibrating sample magnetometry (VSM). Sample preparation was conducted by drop-casting highly concentrated particle dispersions on spherical filter paper (Ø 8 mm) substrates, followed by drying under a high vacuum. Measurements were performed over a magnetic field range of 40 kOe at room temperature and normalized toward the particle weight under compensation of the organic ligand shell.

Magnetic Hyperthermia: Magnetic hyperthermia of phase-transferred particles was investigated over a time span of 10 s under AC magnetic field stimulation at 510 kHz and 20 mT (NAN201003 Magnetherm; nanoTherics Ltd., Warrington, UK). Specific loss power values (SLP) for the different samples were calculated according to the following formula, $SLP = \frac{4.184\ J\ K^{-1}\ mL^{-1}}{m}\frac{dT}{dt}$, in which m is the concentration of the respective particle dispersions in mg mL^{-1}.

Cell Culture: Human Umbilical Vein Endothelial Cells (HUVECs) were cultured following standard procedures. Cells were maintained in Dulbecco's Modified Eagle Medium (DMEM, Gibco) supplemented with 10% Fetal Bovine Serum (FBS) and 1% penicillin/streptomycin for antimicrobial protection. The culture environment was controlled at 37 °C with 5% CO2. The medium was refreshed every 3 days, and cells were passaged biweekly to ensure optimal growth.

Cell Viability Assay: For the experiments, two control groups were established: one consisting solely of HUVECs ("pure cell") and the other comprising only sterile fibrous material ("pure fiber"). Two additional experimental groups involved the incubation of HUVECs with different test materials. All materials intended for cell exposure were sterilized using UV light for 3 h prior to introduction to the cell cultures. Post sterilization, HUVECs were seeded in 24-well plates at a density of 10 000 cells per well, using 1 mL of DMEM. After 24 h, the cells were exposed to the respective test and control materials. This exposure lasted for a period of 48 h to assess the effects of the materials on cell viability. At the end of the incubation period, cell viability was evaluated using the MTT assay.

For the MTT assay, 50 µL of a 3 mg mL^{-1} MTT solution (prepared in Phosphate-Buffered Saline and sourced from Thermo Fisher Scientific) was added to each well. Cells were then incubated for an additional 4 h at 37 °C. Following this incubation, the medium was carefully aspirated, and the formazan crystals formed by viable cells were dissolved in 1 mL of Dimethyl Sulfoxide (DMSO). The absorbance was measured at a wavelength of 570 nm using an Infinite 200 PRO microplate reader (TECAN). Cell viability was then determined and expressed as a percentage in relation to the untreated control cells.

FTIR: FTIR spectra of dried particle powders were measured with a Bruker Tensor 27 spectrometer (Bruker Corp., Billerica, Massachusetts, USA) with a resolution of 4 cm^{-1} across the range of 4000–400 cm^{-1}.

Dynamic Light Scattering and ζ-Potential: Hydrodynamic diameter and ζ-potential of diluted particle dispersions in de-ionized water were determined with a Zetasizer Nano-ZS (Malvern Panalytical GmbH, Kassel, Germany).

Transmission Electron Microscopy (TEM): TEM imaging of NPs was undertaken with a FEI Talos F200X (Chem S/TEM) equipped with a CETA camera (16 M pixel CMOS Camera) and an X-FEG emitter (Thermo Fisher Scientific Inc., Waltham, Massachusetts, USA) operating at 200 kV. Sample preparation was done by dispersing oleic acid-covered NPs in chloroform and drop-casting them into a carbon-coated 400 mesh TEM grid.

TGA: Thermogravimetric measurements were conducted on dried NP powders with a Metter Toledo TGA/DSC 3+ Star up (Mettler-Toledo, Columbus, Ohio, USA) to a temperature of 900 °C under steady airflow.

Scanning Electron Microscopy: Scanning electron microscopy images of the structures were captured using a Zeiss ULTRA 66 (Carl Zeiss GmbH, Oberkochen, Germany) operating at 5 kV. ED elemental mapping was undertaken at 20 kV with a 60 µm aperture and 10 mm working distance.

Magnetic Actuation: Magnetic manipulation of the structures was realized in a custom-made electromagnetic system that consists of eight coils by operating at a magnetic field strength between 5 and 40 mT and a field strength between 50 and 1000 mT m^{-1}.

Mechanical Characterizations of mSCRs: The stiffness measurements were performed with a cellular force microscope (CFM), a microrobotic platform for mechanical characterization of biological samples.[53,54] The CFM has a three-axis positioning system, namely the SmarAct Positioning System (SmarAct Inc., Berkeley, California, USA), with a MEMS capacitive force sensor, namely the FT-S Microforce Sensing Probe (FemtoTools AG, Buchs, Switzerland) with a gain of 49.35 µN V^{-1} and a stiffness of 107.08 N m^{-1}. The system was operated via a LabVIEW program for conducting measurements and gathering data. Before measurements were taken, the system underwent calibration to ensure the sensor tip was within the microscope's field of view. Subsequently, mSCRs were positioned in a small petri dish containing a small amount of water for hydration, along with a minimal amount of detergent to reduce surface tension. Placing the mSCRs directly under the sensor, measurements were initiated by controlling the sensor to descend and capture data. Recorded voltage values and sensor positions were then converted into force-position values. To minimize measurement error, multiple measurements were conducted and averaged. During dehydration and rehydration experiments, mSCRs were transitioned from water to a dry petri dish, and measurements were taken at various intervals. After dehydration, a small amount of water (with minimal detergent) was added, and subsequent time-course stiffness measurements were performed. To model the stiffness of mSCRs, the system comprising the mSCR and sensor was treated as a series of two springs. Employing a simple spring model, stiffness values were extracted from force-position measurements. The stiffness of mSCRs was determined based on the apparent stiffness of the series spring system and the stiffness of the sensor tip.

Supporting Information

Supporting Information is available from the Wiley Online Library or from the author.

Acknowledgements

This work was supported by grants from the Swiss National Science Foundation under project number no. 198643 to U.G. and B.J.N., European Union's Horizon Europe Research and Innovation Programme under EVA project (GA no: 101047081) (J.P.-L. and S.P.), the European Union's Horizon 2020 Proactive Open program under FETPROACT-EIC-05-2019 ANGIE (no. 952152) (J.P.-L. and S.P.), and ETH under grant number 22-2 ETH-040 (S.P.). B.J.N. and S.P. also acknowledge Swiss National Science Foundation (No. 206033) and National Science Foundations of China (Grant 82161138029) for a Sino-Swiss Science and Technology Cooperation project. The Swiss State Secretariat for Education, Research and Innovation (SERI) is also acknowledged. The authors would also like to thank the Scientific Center for Optical and Electron Microscopy (ScopeM) and the FIRST laboratory at ETH for their technical support. J.P.-L. also acknowledges the Agencia Estatal de Investigación (AEI) for the María de Maeztu, project no. CEX2021-001202-M, the grant PID2020-116612RB-C33 funded by MCIN/AEI/10.13039/501100011033, and the Generalitat de Catalunya for the project 2021SGR 00270.

Open access funding provided by Eidgenossische Technische Hochschule Zurich.

Conflict of Interest

F.C.L., B.J.N., and S.P. are planning to establish a startup, Swiss Vascular, which will commercialize the 3D phantom vascular models presented in this contribution.

Data Availability Statement

The data that support the findings of this study are available from the corresponding author upon reasonable request.

Keywords

magnetic soft continuum robots, microfluidics, multifunctionality, reaction-diffusion controlled fabrication, shape transformation, tailored magnetic actuation

Received: February 13, 2024
Revised: May 15, 2024
Published online:

[1] B. J. Nelson, S. Pané, *Science* **2023**, *382*, 1120.
[2] S. Palagi, P. Fischer, *Nat. Rev. Mater.* **2018**, *3*, 113.
[3] L. da Vinci, Codex on the Flight of Birds Pdf. Retrieved from the Library of Congress, **1505**, https://www.loc.gov/item/2021668201.
[4] N. Shamsudhin, N. Laeubli, H. B. Atakan, H. Vogler, C. Hu, W. Haeberle, A. Sebastian, U. Grossniklaus, B. J. Nelson, *PLoS One* **2016**, *11*, e0168138.
[5] J.-M. Volland, S. Gonzalez-Rizzo, O. Gros, T. Tyml, N. Ivanova, F. Schulz, D. Goudeau, N. H. Elisabeth, N. Nath, D. Udwary, R. R. Malmstrom, C. Guidi-Rontani, S. Bolte-Kluge, K. M. Davies, M. R. Jean, J.-L. Mansot, N. J. Mouncey, E. R. Angert, T. Woyke, S. V. Date, *Science* **2022**, *376*, 1453.
[6] A. Sadeghi, A. Mondini, B. Mazzolai, *Soft Rob.* **2017**, *4*, 211.
[7] E. W. Hawkes, L. H. Blumenschein, J. D. Greer, A. M. Okamura, *Sci. Rob.* **2017**, *2*, eaan3028.
[8] N. D. Naclerio, A. Karsai, M. Murray-Cooper, Y. Ozkan-Aydin, E. Aydin, D. I. Goldman, E. W. Hawkes, *Sci. Rob.* **2021**, *6*, eabe2922.
[9] M. M. Hausladen, B. Zhao, M. S. Kubala, L. F. Francis, T. M. Kowalewski, C. J. Ellison, *Proc. Natl. Acad. Sci. USA* **2022**, *119*, 2201776119.
[10] C. Chautems, A. Tonazzini, Q. Boehler, S. H. Jeong, D. Floreano, B. J. Nelson, *Adv. Intell. Syst.* **2020**, *2*, 1900086.
[11] J. Lussi, M. Mattmann, S. Sevim, F. Grigis, C. De Marco, C. Chautems, S. Pané, J. Puigmartí-Luis, Q. Boehler, B. J. Nelson, *Adv. Sci.* **2021**, *8*, 2101290.
[12] M. Mattmann, C. De Marco, F. Briatico, S. Tagliabue, A. Colusso, X. Chen, J. Lussi, C. Chautems, S. Pané, B. Nelson, *Adv. Sci.* **2022**, *9*, 2103277.
[13] H. Gu, E. Hanedan, Q. Boehler, T.-Y. Huang, A. J. T. M. Mathijssen, B. J. Nelson, *Nat. Mach. Intell.* **2022**, *4*, 678.
[14] H.-W. Huang, M. S. Sakar, A. J. Petruska, S. Pané, B. J. Nelson, *Nat. Commun.* **2016**, *7*, 12263.
[15] E. Kang, G. S. Jeong, Y. Y. Choi, K. H. Lee, A. Khademhosseini, S.-H. Lee, *Nat. Mater.* **2011**, *10*, 877.
[16] I. W. Hamley, *Angew. Chem., Int. Ed.* **2003**, *42*, 1692.
[17] R. M. Erb, H. S. Son, B. Samanta, V. M. Rotello, B. B. Yellen, *Nature* **2009**, *457*, 999.
[18] Y.-Y. Xiao, Z.-C. Jiang, Y. Zhao, *Adv. Intell. Syst.* **2020**, *2*, 2000148.
[19] C. Hu, S. Pané, B. J. Nelson, *Annu. Rev. Control Rob. Auton. Syst.* **2018**, *1*, 53.
[20] T.-Y. Huang, H. Gu, B. J. Nelson, *Annu. Rev. Control Rob. Auton. Syst.* **2022**, *5*, 279.
[21] C. Zhang, D. A. Mcadams, J. C. Grunlan, *Adv. Mater.* **2016**, *28*, 6292.
[22] M. Liu, S. Wang, L. Jiang, *Nat. Rev. Mater.* **2017**, *2*, 17036.
[23] S. B. Primrose, *Biomimetics: Nature-Inspired Design and Innovation*, Wiley, Hoboken, NJ **2020**.
[24] N. K. Katiyar, G. Goel, S. Hawi, S. Goel, *NPG Asia Mater.* **2021**, *13*, 56.
[25] M. Albéric, M. N. Dean, A. Gourrier, W. Wagermaier, J. W. C. Dunlop, A. Staude, P. Fratzl, I. Reiche, *PLoS One* **2017**, *12*, e0166671.
[26] P. Monnard, D. W. Deamer, *Anat. Rec.* **2002**, *268*, 196.
[27] A. Pohorille, D. Deamer, *Res. Microbiol.* **2009**, *160*, 449.
[28] G. M. Whitesides, B. Grzybowski, *Science* **2002**, *295*, 2418.
[29] Y. Deng, Y. Zhao, J. Zhang, T. Arai, Q. Huang, X. Liu, *Adv. Intell. Syst.* **2024**, *6*, 2300471.
[30] S. E. Chung, W. Park, S. Shin, S. A. Lee, S. Kwon, *Nat. Mater.* **2008**, *7*, 581.
[31] Y. Dou, B. Wang, M. Jin, Y. Yu, G. Zhou, L. Shui, *J. Micromech. Microeng.* **2017**, *27*, 113002.
[32] S. Sevim, A. Sorrenti, C. Franco, S. Furukawa, S. Pané, A. J. deMello, J. Puigmartí-Luis, *Chem. Soc. Rev.* **2018**, *47*, 3788.
[33] Z. Wei, S. Wang, J. Hirvonen, H. A. Santos, W. Li, *Adv. Healthcare Mater.* **2022**, *11*, 2200846.
[34] Y. Dong, L. Wang, V. Iacovacci, X. Wang, L. Zhang, B. J. Nelson, *Matter* **2022**, *5*, 77.
[35] K. P. Yuet, D. K. Hwang, R. Haghgooie, P. S. Doyle, *Langmuir* **2010**, *26*, 4281.
[36] S. Lone, I. W. Cheong, *RSC Adv.* **2014**, *4*, 13322.
[37] Y. Cheng, F. Zheng, J. Lu, L. Shang, Z. Xie, Y. Zhao, Y. Chen, Z. Gu, *Adv. Mater.* **2014**, *26*, 273.
[38] Y. Yu, F. Fu, L. Shang, Y. Cheng, Z. Gu, Y. Zhao, *Adv. Mater.* **2017**, *29*, 1605765.
[39] Y. Yu, L. Shang, W. Gao, Z. Zhao, H. Wang, Y. Zhao, *Angew. Chem., Int. Ed.* **2017**, *56*, 12127.
[40] Y. Liu, Y. Yang, X. Yang, L. Yang, Y. Shen, W. Shang, *J. Mater. Chem. B* **2021**, *9*, 1441.
[41] H. Onoe, T. Okitsu, A. Itou, M. Kato-Negishi, R. Gojo, D. Kiriya, K. Sato, S. Miura, S. Iwanaga, K. Kuribayashi-Shigetomi, Y. T. Matsunaga, Y. Shimoyama, S. Takeuchi, *Nat. Mater.* **2013**, *12*, 584.
[42] W. Liu, Z. Zhong, N. Hu, Y. Zhou, L. Maggio, A. K. Miri, A. Fragasso, X. Jin, A. Khademhosseini, Y. S. Zhang, *Biofabrication* **2018**, *10*, 024102.
[43] S. Hassan, E. Gomez-Reyes, E. Enciso-Martinez, K. Shi, J. G. Campos, O. Y. P. Soria, E. Luna-Cerón, M. C. Lee, I. Garcia-Reyes, J. Steakelum, H. Jeelani, L. E. García-Rivera, M. Cho, S. S. Cortes, T. Kamperman, H. Wang, J. Leijten, L. Fiondella, S. R. Shin, *ACS Appl. Mater. Interfaces* **2022**, *14*, 51602.
[44] C. Richard, A. Neild, V. J. Cadarso, *Lab Chip* **2020**, *20*, 2044.
[45] Q. Zhao, H. Cui, Y. Wang, X. Du, *Small* **2020**, *16*, 1903798.
[46] L. A. Jaffe, M. H. Weisenseel, L. F. Jaffe, *J. Cell Biol.* **1975**, *67*, 488.
[47] R. Malho, N. D. Read, M. S. Pais, A. J. Trewavas, *Plant J.* **1994**, *5*, 331.
[48] M. Diao, X. Qu, S. Huang, *J. Integr. Plant Biol.* **2018**, *60*, 897.
[49] E. Michard, A. A. Simon, B. Tavares, M. M. Wudick, J. A. Feijó, *Plant Physiol.* **2017**, *173*, 91.
[50] K. Y. Lee, D. J. Mooney, *Prog. Polym. Sci.* **2012**, *37*, 106.
[51] F. C. Landers, V. Gantenbein, L. Hertle, A. Veciana, J. Llacer-Wintle, X. Chen, H. Ye, C. Franco, J. Puigmartí-Luis, M. Kim, B. J. Nelson, S. Pané, *Adv. Mater.* **2024**, *36*, 2310084.
[52] L. Nie, P. Chang, C. Ji, F. Zhang, Q. Zhou, M. Sun, Y. Sun, C. Politis, A. Shavandi, *Colloids Surf., B* **2021**, *197*, 111385.
[53] D. Felekis, H. Vogler, G. Mecja, S. Muntwyler, A. Nestorova, T. Huang, M. S. Sakar, U. Grossniklaus, B. J. Nelson, *Int. J. Rob. Res.* **2015**, *34*, 1136.

[54] J. T. Burri, C. Hu, N. Shamsudhin, X. Wang, H. Vogler, U. Grossniklaus, B. J. Nelson, in *2016 IEEE International Conference on Automation Science and Engineering (CASE)*, IEEE, Fort Worth, TX **2016**, pp. 942–947.
[55] Y. Chen, T. Liang, L. Chen, Y. Chen, B.-R. Yang, Y. Luo, G.-S. Liu, *Nanoscale Horiz.* **2022**, *7*, 1299.
[56] J. M. D. Coey, *Phys. Rev. Lett.* **1971**, *27*, 1140.
[57] S. Linderoth, P. V. Hendriksen, F. Bo/dker, S. Wells, K. Davies, S. W. Charles, S. Mo/rup, *J. Appl. Phys.* **1994**, *75*, 6583.
[58] A. E. Deatsch, B. A. Evans, *J. Magn. Magn. Mater.* **2014**, *354*, 163.
[59] B. Chueh, Y. Zheng, Y. Torisawa, A. Y. Hsiao, C. Ge, S. Hsiong, N. Huebsch, R. Franceschi, D. J. Mooney, S. Takayama, *Biomed. Microdevices* **2010**, *12*, 145.